

# Simulation of particle deposition beneath Faraday waves in thin liquid films

J. R. Saylor<sup>a)</sup> and A. L. Kinard

*Department of Mechanical Engineering, Clemson University, Clemson, South Carolina 29634*

(Received 28 May 2004; accepted 1 February 2005; published online 31 March 2005)

Simulations are presented of particle deposition beneath shallow, standing capillary waves. The standing waves occur on the surface of a thin liquid film. The film is sufficiently thin such that the wave motion affects the trajectories of the settling particles. The simulations reveal that particles of all size tend to accumulate at specific nodal regions beneath the waves, and that there is an optimal particle diameter for which this accumulation is maximized. The diameter at which this maximal accumulation occurs is a function of the wave field, the fluid thickness, the particle density, and the fluid properties. The accumulation is quantified by the standard deviation of the final location of the settling particles and plots are presented of this standard deviation as a function of particle diameter. Previous experimental work has shown that this method can be implemented by generating standing Faraday waves on the surface of thin films of a liquid/particulate mixture. The present work shows how these films can be tailored via the particle diameter, liquid thickness, and wavelength. Some aspects relevant to the practical implementation of the method are also discussed. © 2005 American Institute of Physics. [DOI: 10.1063/1.1884111]

## I. INTRODUCTION

Standing waves create a velocity field beneath the water surface that can influence the motion of settling particles. Because the velocity field decays rapidly with depth, it has a minimal effect on the pattern of particulate deposition on the bottom boundary when the water is deep (i.e., the water depth is greater than a few wavelengths). However for the shallow wave case the wave motion affects significantly the velocity field at locations ranging from the liquid surface all the way to the bottom boundary. At the bottom boundary, the existence of a no-slip boundary condition combined with the oscillatory wave motion results in oscillatory boundary layers which have a significant effect on the ultimate location of settling particles.

In our earlier work we presented the equations for the oscillatory boundary layers for shallow standing waves showing that settling particles should collect at specific accumulation points.<sup>1</sup> We then presented experiments where standing capillary waves were created on thin liquid films in the form of Faraday waves. The wavelength and film thickness were both about a millimeter. Talc particles suspended in this thin liquid film deposited in a pattern that mirrored the standing wave field, demonstrating that this method can be applied in practice to create patterned, particulate films, which we referred to as “Faraday films.” A simple simulation of the particle deposition was presented in that earlier work. Herein we present a more sophisticated and detailed simulation of the particle deposition showing the effect of particle diameter and liquid film thickness. Water is the working fluid in all simulations.

A recapitulation is now presented of the equations describing the velocity field beneath shallow capillary waves,

presented in Wright and Saylor.<sup>1</sup> This is a synthesis of the equations initially developed by Miche,<sup>2</sup> Lin *et al.*,<sup>3</sup> and Noda.<sup>4</sup>

### A. The velocity field beneath a standing wave

A second-order potential flow solution for the velocity field ( $u, v$ ) beneath finite depth standing waves, was developed by Miche,<sup>2</sup>

$$u(x, y) = 2hb \frac{\cosh[a(H - y)]}{\sinh(aH)} \cos(ax) \cos(bt) + \frac{3}{2} \frac{h^2 ab}{\sinh^4(aH)} \cosh[2a(H - y)] \sin(2ax) \sin(2bt), \quad (1)$$

$$v(x, y) = -2hb \frac{\sinh[a(H - y)]}{\sinh(aH)} \sin(ax) \cos(bt) + \frac{3}{2} \frac{h^2 ab}{\sinh^4(aH)} \sinh[2a(H - y)] \cos(2ax) \sin(2bt), \quad (2)$$

where  $H$  is the thickness of the liquid layer,  $2h$  is the wave amplitude,  $x$  is the lateral dimension,  $\lambda$  is the wavelength,  $a = 2\pi/\lambda$ ,  $\tau$  is the wave period,  $b = 2\pi/\tau$ , and  $y = -z$  is the distance from the flat water surface into the fluid ( $y$  is positive in the downward direction). Equations (1) and (2) provide accurate velocities away from the bottom boundary. However, because they are potential flow solutions, they fail to predict the existence of boundary layers near the bottom boundary. Lin *et al.*<sup>3</sup> developed a solution for the  $u$ -direction velocity field in these boundary layers using Miche's second-order inviscid solution<sup>2</sup> and the work of Noda,<sup>4</sup>

<sup>a)</sup> Author to whom correspondence should be addressed. Electronic mail: jrsaylor@ces.clemson.edu

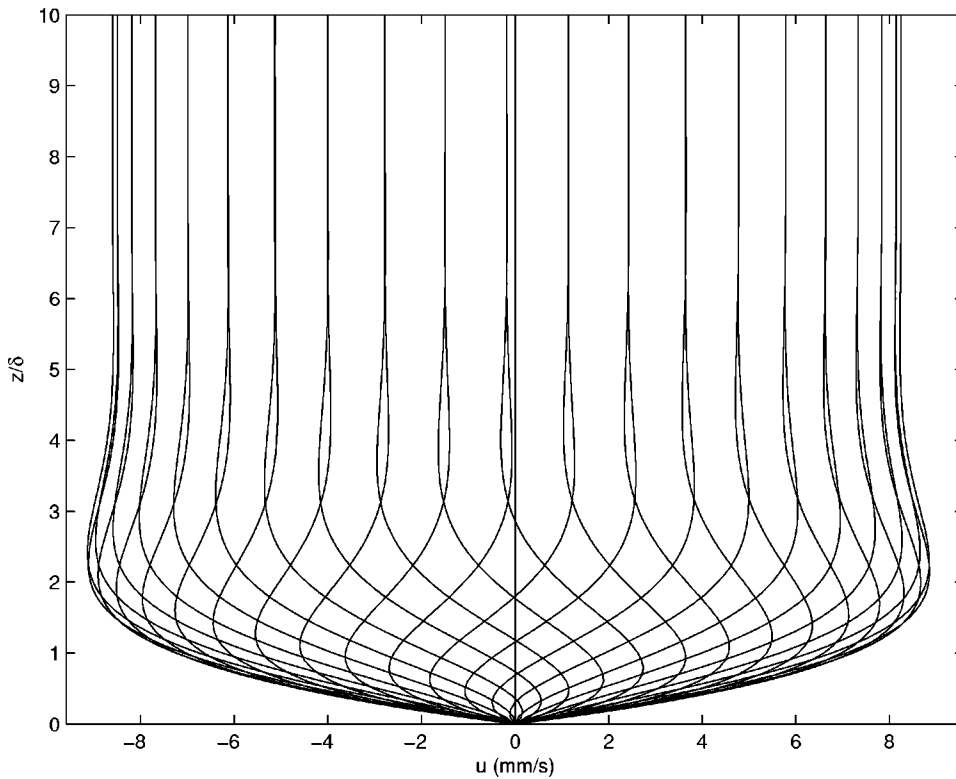


FIG. 1. Boundary layer profiles at  $x = \lambda/8$  plotted over a single wave period.

$$\begin{aligned}
 \frac{u}{u_{\delta m}} = & -\sin(ax) \left[ \cos(bt) - e^{-z/\delta} \cos\left(bt - \frac{z}{\delta}\right) \right] + \frac{4h}{L} \left\{ \frac{-3\pi \cos(2ax)}{8 \sinh^3(aH)} \left[ \sin(2bt) - e^{-\sqrt{2}z/\delta} \sin\left(2bt - \sqrt{2}\frac{z}{\delta}\right) \right] \right. \\
 & + \frac{\pi \sin(2ax)}{4 \sinh(aH)} \sin(2bt) \cdot \left[ e^{-\sqrt{2}z/\delta} \cos\left(\sqrt{2}\frac{z}{\delta}\right) - e^{-z/\delta} \cos\left(\frac{z}{\delta}\right) + \frac{\sqrt{2}z}{\delta} e^{-z/\delta} \sin\left(\frac{z}{\delta} + \frac{\pi}{4}\right) \right] + \frac{\pi \sin(2ax)}{4 \sinh(aH)} \cos(2bt) \\
 & \cdot \left[ -e^{-\sqrt{2}z/\delta} \sin\left(\sqrt{2}\frac{z}{\delta}\right) + e^{-z/\delta} \sin\left(\frac{z}{\delta}\right) + \frac{\sqrt{2}z}{\delta} e^{-z/\delta} \cos\left(\frac{z}{\delta} + \frac{\pi}{4}\right) \right] + \frac{\pi \sin(2ax)}{8 \sinh(aH)} \left[ -3 + e^{-2z/\delta} + 8e^{-z/\delta} \sin\left(\frac{z}{\delta}\right) \right. \\
 & \left. \left. + 2e^{-z/\delta} \cos\left(\frac{z}{\delta}\right) - 2\sqrt{2}\frac{z}{\delta} e^{-z/\delta} \cos\left(\frac{z}{\delta} + \frac{\pi}{4}\right) \right] \right\}. \quad (3)
 \end{aligned}$$

Here  $u_{\delta m}$  is the maximum velocity (the velocity outside the boundary layer),

$$u_{\delta m} = \frac{2bh}{\sinh(aH)}, \quad (4)$$

$\delta$  is the Stokes characteristic length,

$$\delta = \sqrt{\frac{2\nu}{b}}, \quad (5)$$

$\nu$  is the kinematic viscosity and  $z$  is the distance from the bottom boundary [note that in Eq. (3) the sense of  $z$  is opposite that used in Eqs. (1) and (2)]. Equation (3) provides the oscillating boundary layer profile ( $u$  versus  $z$ ) at different lateral points beneath the wave.

Boundary layer profiles are presented in Figs. 1–3 for  $x = \lambda/8$ ,  $\lambda/2$ , and  $7\lambda/8$ , respectively. In each figure, 40 profiles are plotted over the entire wave cycle (only 20 are vis-

ible in Fig. 2 due to overlapping during the course of a single wave cycle). Note that in Fig. 1 the profiles exhibit a slight leftward asymmetry, in Fig. 2 the profiles are symmetric about the vertical axis, and in Fig. 3 they exhibit a slight rightward asymmetry. The  $x$  locations which exhibit an asymmetric set of boundary layer profiles are locations where there is a net horizontal flow of fluid over an integral number of wave cycles in the thin liquid film. Figure 4 presents this net flow as a function of  $x$ . The values presented in this figure were obtained by integrating the boundary layer profiles over one wave period. In the computations used to create Figs. 1–4, the working fluid was water and the parameters were  $\lambda = 5$  mm, the fluid thickness was  $0.55\lambda$  (2.75 mm), and the wave amplitude was  $\lambda/10$  (0.5 mm). Note that these numbers differ slightly from the work of Wright and Saylor,<sup>1</sup> where the fluid thickness was 2.5 mm.

Figure 4 shows that there are regions beneath the wave where the net flow results in a collection point. For example,

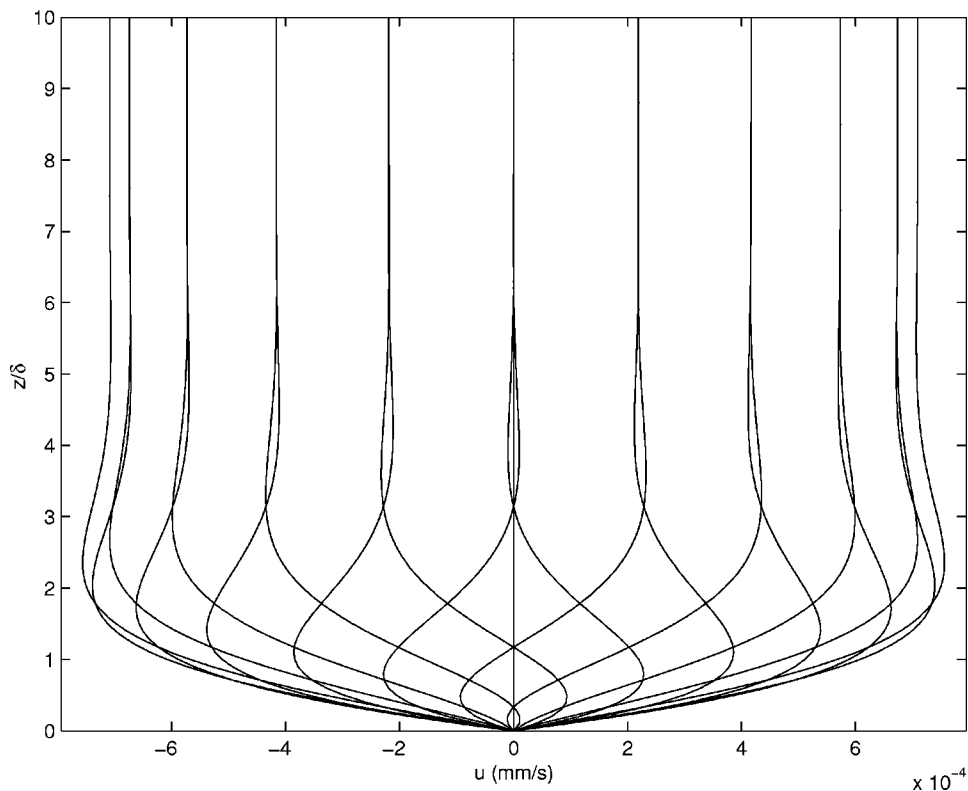


FIG. 2. Boundary layer profiles at  $x = \lambda/2$  plotted over a single wave period.

at  $x = \lambda/2$ , the flow is negative to the right of this point and positive to the left of this point, indicating that a particle in this locale would migrate toward  $\lambda/2$  as it settled. In contrast at locations such as  $x = \lambda/4$ , the flow is negative to the left of this point and positive to the right of this point, which would cause particles to be swept outward from this point. The

experiments presented in Wright and Saylor<sup>1</sup> confirmed the existence of the aforementioned accumulation points. This work indicated that settling particles deposited in patterned films where the two-dimensional pattern of collection points mimicked the standing wave field (Faraday waves in this case) that existed on the liquid surface. A sample image of

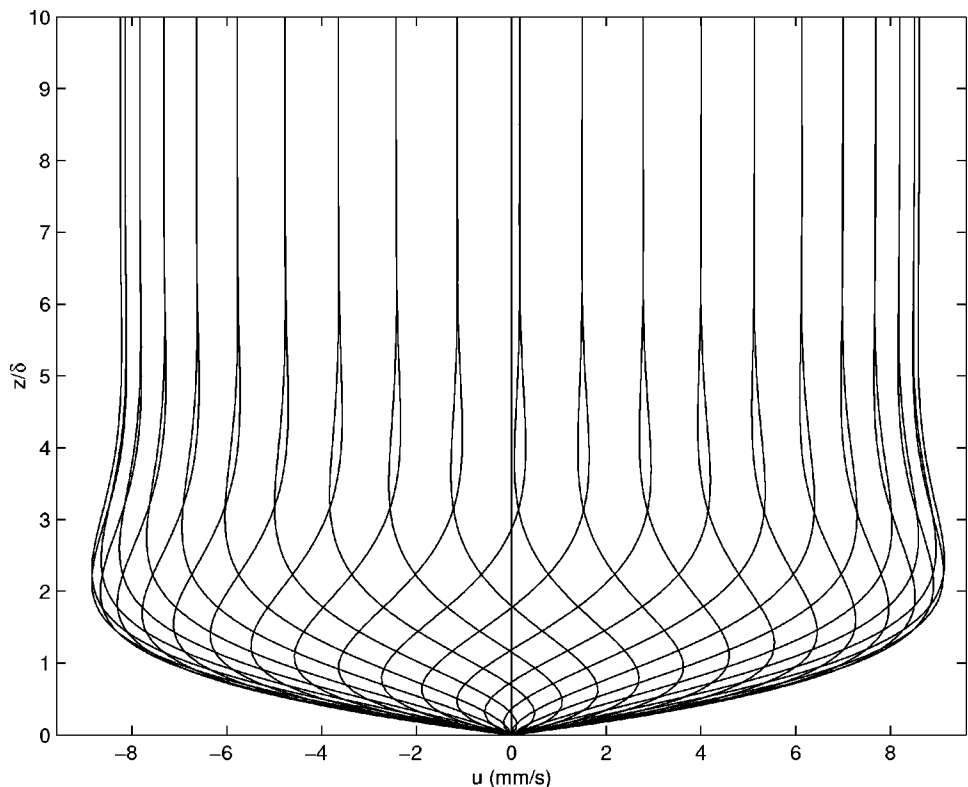


FIG. 3. Boundary layer profiles at  $x = 7\lambda/8$  plotted over a single wave period.

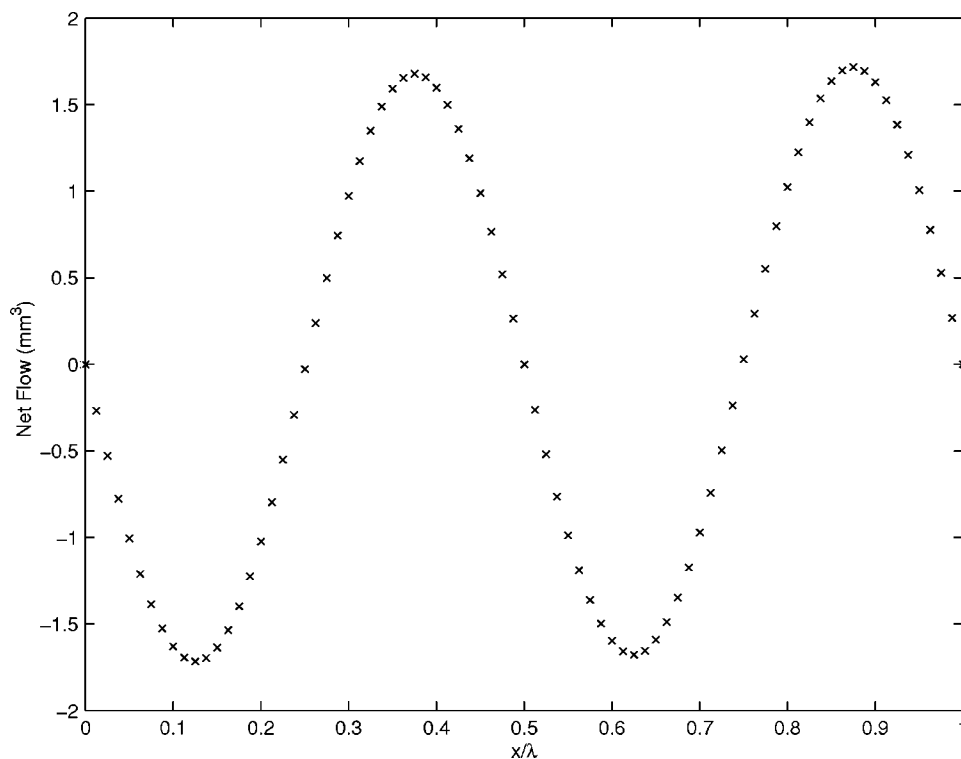


FIG. 4. Plot of the net flow vs  $x$  location. The net flow is obtained by integrating the boundary layer profiles over a complete wave cycle. Integration is performed over a unit depth and over  $10\delta$  of the boundary layer thickness.

such a pattern is presented in Fig. 5. This image of the dried particulate film appears very much like the Faraday wave field that produced it.

The ability to create patterned particulate films is important in several fields. One area is the generation of templates for the development of scaffolds in tissue engineering, where these scaffolds serve as a support structure during tissue growth.<sup>5</sup> The Faraday films described here may be used to create such scaffolds via the repetitive deposition of these particulate films. Another application of Faraday films is in nanoscience where the manipulation of nanoparticles shows

great promise to a variety of applications.<sup>6,7</sup> An ability to attain better control over the quality of Faraday films like those presented in Fig. 5 may enable the development of nanoparticulate films. Deposition of particulate photonic materials in regular patterns is critical to the development of flat panel displays and other display technologies providing yet another application of the Faraday films described herein.<sup>8</sup> Finally, the characterization of potential catalytic materials requires the controlled deposition of particles in a structured pattern which may be achieved using Faraday films.<sup>9</sup>

## B. Control of particulate films

The patterns generated in Faraday films can be controlled in several ways. First, the resulting particulate pattern mirrors the standing wave field, and the wavelength of the particulate pattern can be changed simply by changing the wavelength of the Faraday waves excited on the liquid surface. This can be done by varying the excitation frequency, providing a very simple means of controlling the particulate pattern scale. Even finer control of the particulate pattern may also be attainable. A particle settling through the oscillatory boundary layers shown in Figs. 1–3 will experience a fall path, or trajectory, that depends on its initial  $x$  location, diameter, density, the wave field and the liquid film thickness. For example, Fig. 6 shows how the net flow can be varied with the fluid thickness (all other variables being held constant). This plot indicates that for constant wave amplitude, the magnitude of the net flow decreases as the fluid thickness increases. Since this flow determines, partially, the final location of the particles, the fluid thickness can be used as a tuning parameter to adjust the characteristics of the resulting particulate film. Another way in which the particulate

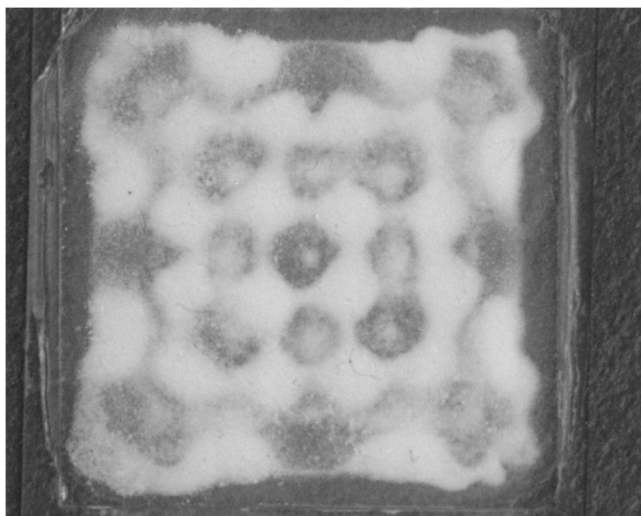


FIG. 5. Sample image of a particulate film created when talc particles settled in a thin film of water having a standing field of Faraday waves on its surface. The talc covered region is  $22 \times 22$  mm<sup>2</sup> in extent. Obtained from Wright and Saylor (Ref. 1).

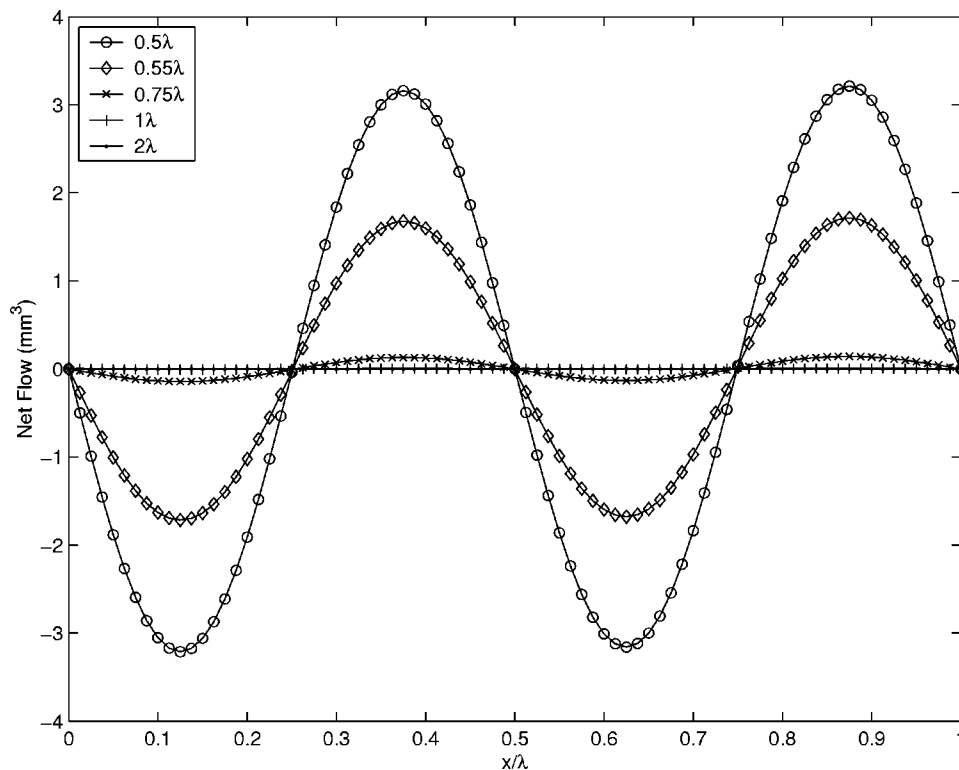


FIG. 6. Plots of the net flow vs  $x$  location for a range of fluid thickness. The symbols presented in the legend are the thickness of the liquid film. The integration used to obtain the net flow is the same as that described in Fig. 4.

film characteristics can be tailored is by changing the particle diameter. As the particle diameter increases, the degree to which it follows the oscillatory flow changes, causing particles of different diameter to settle in different locations, even if they start at the same initial position. The ability to tailor characteristics of the particulate film by changing the thickness of the liquid film or the diameter of the settling particles has not been addressed and is the subject of the present work.

Patterning particulate films as the particle size gets very small raises a problem concerning the ability of the particles to settle. The particles used in creating the sample film presented in Fig. 5, were relatively large talc particles that settled quickly. Very small particles will not settle due to gravitational forces alone in any reasonable period of time. Accordingly, an alternative settling force must be implemented, such as an electric field. In this scenario, the settling velocity would be controlled by the field strength. Normally, when particles settle due to gravity, the time that a particle would spend in the oscillatory boundary layer is determined by the particle mass and diameter, which would determine its terminal velocity. However, if the particles are forced to settle via a user-controlled velocity, the time that the particles spend in the oscillatory field is set by the user. In the work presented herein, the particle settling rate is arbitrarily set, for each film thickness considered, so that all particles settle at the same rate, regardless of their diameter or density. In this way the effect of the oscillatory velocity field is separated from the effect of terminal velocity which, as noted above, may be arbitrary.

In the following section the computational method used to simulate the deposition of particles is described. The trajectories of a set of particles are simulated, and the results of

these simulations are then presented. Parameters which are varied in these simulations are particle diameter and film thickness. The wavelength  $\lambda$  is set to a fixed fraction of the film thickness, so while  $\lambda$  changes for each case, it is not an independently varied parameter. The reason for keying film thickness to wavelength is that the fluid flow caused by the standing waves is only significant near the bottom boundary when the liquid thickness is comparable to the wavelength. Having liquid thicknesses several  $\lambda$  in extent would have minimal effect on particulate deposition.

## II. COMPUTATIONAL METHOD

To study the deposition behavior of particles beneath a standing wave field, a set of initial locations was required for the particles considered. Because the net transport of particles is due to the asymmetries of the oscillatory boundary layers that are prominent near the bottom boundary, an array of particle initial conditions was located just outside of the boundary layer region. Ninety particles were investigated, organized initially in a rectangular grid, as shown in Fig. 7(a).

Two particle types were considered. The first particle type has a density twice that of water, which is the liquid used in all simulations. These are referred to as “SG2 particles” hereinafter since they have a specific gravity of two. A range of particle diameters were considered for the SG2 particles. The second particle type considered were massless particles, i.e., particles that followed the flow perfectly and settled at the same rate as the SG2 particles. These massless particles show the limiting case of an actual particle as its mass approaches zero. The goal of these simulations was to

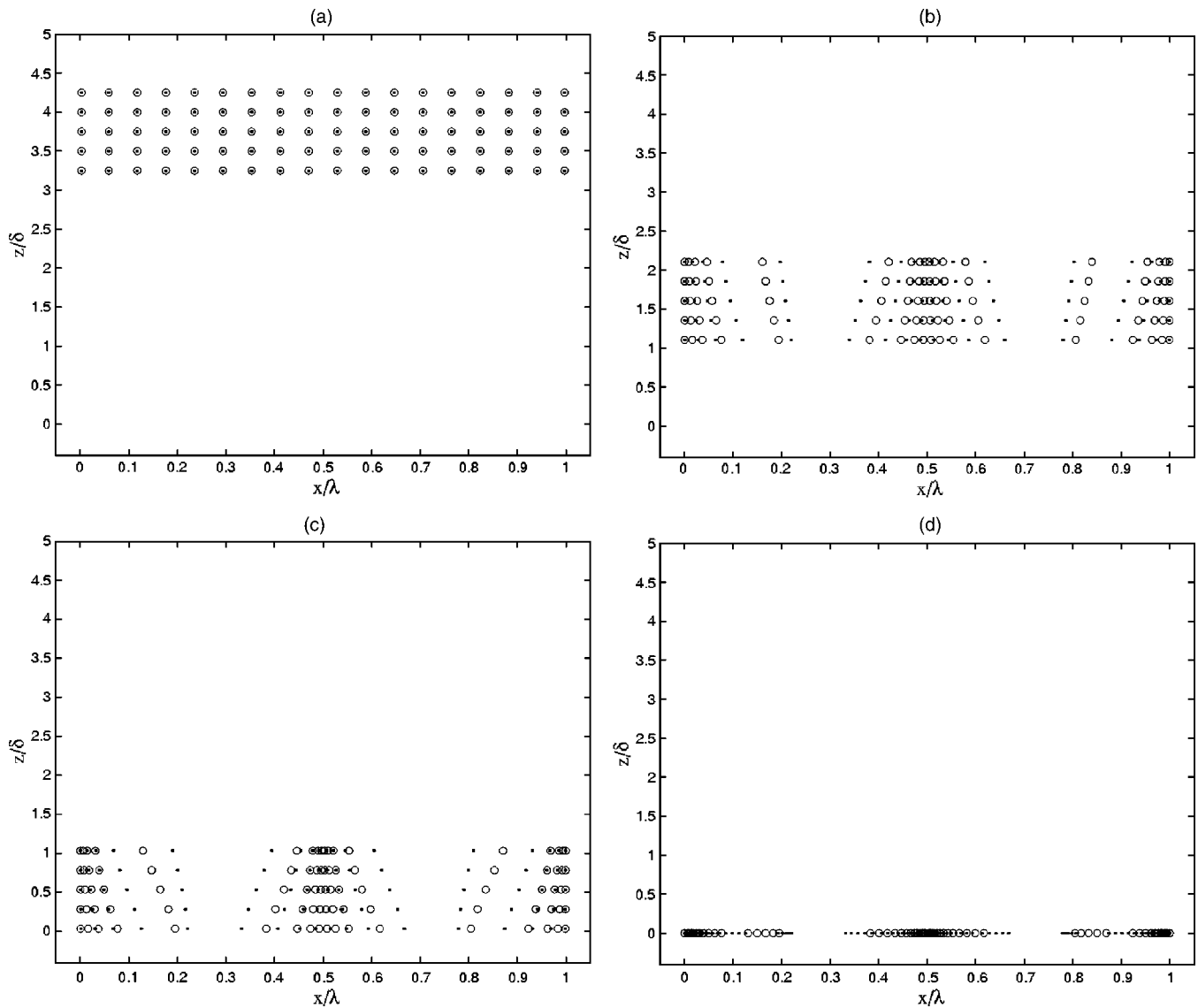


FIG. 7. Locations of massless (●) and SG2 (○) particles. (a) Initial locations of particles, (b) after 200 wave cycles, (c) after 300 wave cycles, and (d) after 400 wave cycles. In this sample simulation,  $\lambda=5$  mm and the diameter of the SG2 particles was  $170 \mu\text{m}$ .

show the effect of particle diameter on the deposition pattern of SG2 particles. The massless particles are used as a baseline for comparison.

As described in Sec. I, the settling velocity for all particles is artificially set so that all particles spend the same amount of time in the oscillatory boundary layer. Hence, the time required for the particle to “fall” to the solid substrate is not determined by the particle mass and diameter as would normally be the case. In this way we separate out the settling time effect on the resulting deposition pattern. The settling speed was set so that the upper layer of particles fell to the solid substrate in 400 wave cycles. Since the upper layer of particles was located at  $z=4.25\delta$ , the settling speed was

$$v_s = \frac{4.25 \delta}{400 \tau}. \tag{6}$$

The choice of 400 cycles was made based on a trade-off between computational efficiency and permitting a significant amount of particle accumulation (the longer the par-

ticles reside in the boundary layers, the greater the degree of accumulation).

Since there are no inertial effects present for the massless particles, their positions were determined by a simple forward differencing of the velocity field. Hence, the  $x$  and  $y$  locations of the massless particles  $(x_m, y_m)$  were determined by

$$x_m(t + \Delta t) = x_m(t) + u(x_m, y_m)\Delta t \tag{7}$$

and

$$y_m(t + \Delta t) = y_m(t) + v_s(x_m, y_m)\Delta t, \tag{8}$$

where  $u$  is determined from Eq. (3) and  $v_s$  from Eq. (6). For the SG2 particles, the particle positions  $(x_p, y_p)$  were determined as follows. First the drag on the particle was computed according to

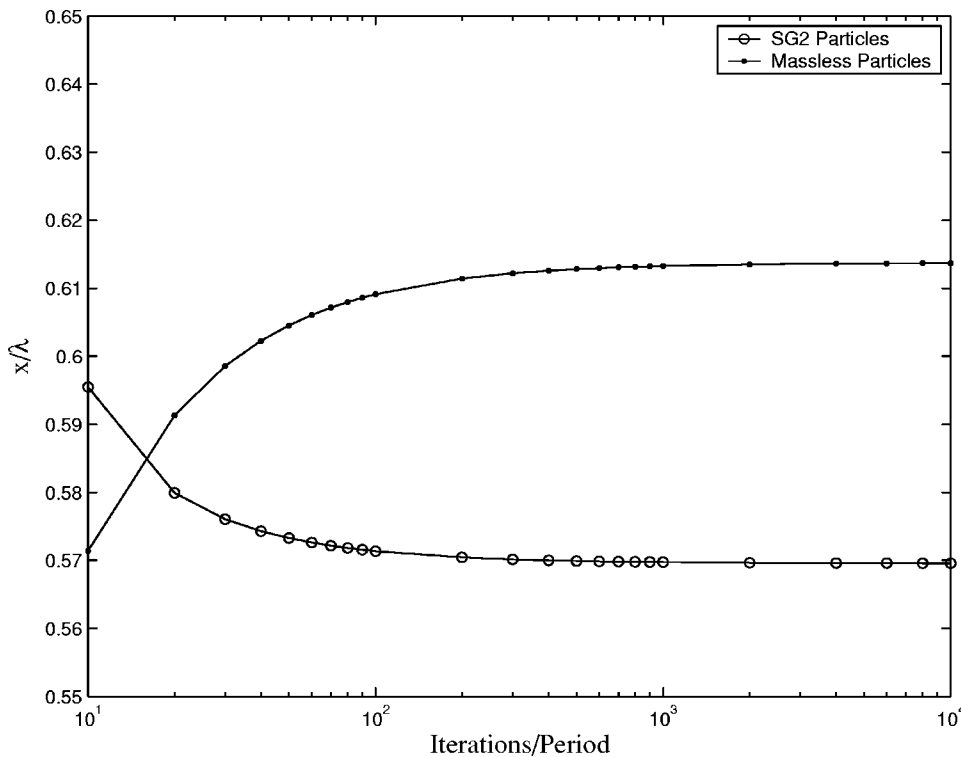


FIG. 8. Plot showing the final deposition  $x$  location of a massless particle and the SG2 particle as a function of the number of iterations per wave period. The diameter of the SG2 particle was  $100 \mu\text{m}$ . This was for  $\lambda=5 \text{ mm}$  and a fluid thickness of  $2.75 \text{ mm}$ .

$$F_d(x_p, y_p) = \frac{1}{2} \rho C_d A |u_\Delta| u_\Delta, \quad (9)$$

where  $u_\Delta$  is the difference between the particle and fluid velocities,

$$u_\Delta(x_p, y_p) = u(x_p, y_p) - u_p(x_p, y_p), \quad (10)$$

$u_p$  is the  $x$  component of the particle velocity,  $u$  is the fluid velocity according to Eq. (3), and  $A$  is the projected area of the spherical particle.  $C_d$  is defined as<sup>10</sup>

$$C_d = \frac{24}{\text{Re}} + \frac{6}{(1 + \sqrt{\text{Re}})} + 0.4, \quad (11)$$

where  $\text{Re}$  is the Reynolds number based on the particle diameter:

$$\text{Re} = \frac{u_\Delta d}{\nu}. \quad (12)$$

Equation (11) is valid for  $0 \leq \text{Re} \leq 2 \times 10^5$ . The  $x$ -direction SG2 particle acceleration  $a_p$  was then computed according to

$$a_p(x_p, y_p) = F_d(x_p, y_p) / m_p, \quad (13)$$

where  $m_p$  is the mass of the particle. The SG2 particle velocity  $u_p$  and position  $x_p$  were updated by forward differencing according to

$$u_p(t + \Delta t) = u_p(t) + a_p(x_p, y_p) \Delta t \quad (14)$$

and

$$x_p(t + \Delta t) = x_p(t) + u_p(x_p, y_p) \Delta t. \quad (15)$$

The  $y$  locations of the SG2 particles are determined as for the massless particles, namely,

$$y_p(t + \Delta t) = y_p(t) + v_s(x_p, y_p) \Delta t. \quad (16)$$

Simulation of the above equations provides an accurate trajectory of the particle paths, assuming that the forces acting on the particles are due solely to drag from the surrounding fluid. It is implicitly assumed that other influences do not occur, such as particle-particle interactions, investigated, for example, by Voth *et al.*<sup>11</sup> Hence, the simulations presented here may not be accurate in high-concentration slurries. Also ignored are shear induced particle motion such as that investigated by Eckstein *et al.*<sup>12</sup> and Leighton and Acrivos.<sup>13-15</sup> This is left for future work.

For all of the simulations presented here, the wave amplitude was  $2h=0.1\lambda$ , the liquid thickness was  $H=0.55\lambda$ , and the liquid was water. A characteristic velocity can be computed as  $2hf$  where  $f$  is the wave frequency, computed from the shallow water limit of the dispersion relationship for capillary waves,

$$f = \frac{2\pi}{\lambda^2} \sqrt{\frac{\gamma H}{\rho}} \quad (17)$$

where  $H$  is the liquid layer thickness,  $\gamma$  is the liquid surface tension, and  $f$  is the wave frequency.<sup>16</sup> Using this characteristic velocity, a value for  $\text{Re}$  can be computed for each of the particle diameters computed. This value of  $\text{Re}$  was less than  $2 \times 10^5$  for all wavelengths and particle diameters presented here. Hence, Eq. (11) is valid for the results presented herein.

Smaller particle diameters required smaller values of  $\Delta t$  to maintain computational stability. The range of  $\Delta t$  was  $\tau/100\,000 < \Delta t < \tau/750$ . The appropriate value was determined by convergence plots, an example of which is presented in Fig. 8 which shows the final deposition location of a particle as a function of the number of iterations per wave period. For this particular particle diameter ( $d=100 \mu\text{m}$ ) and

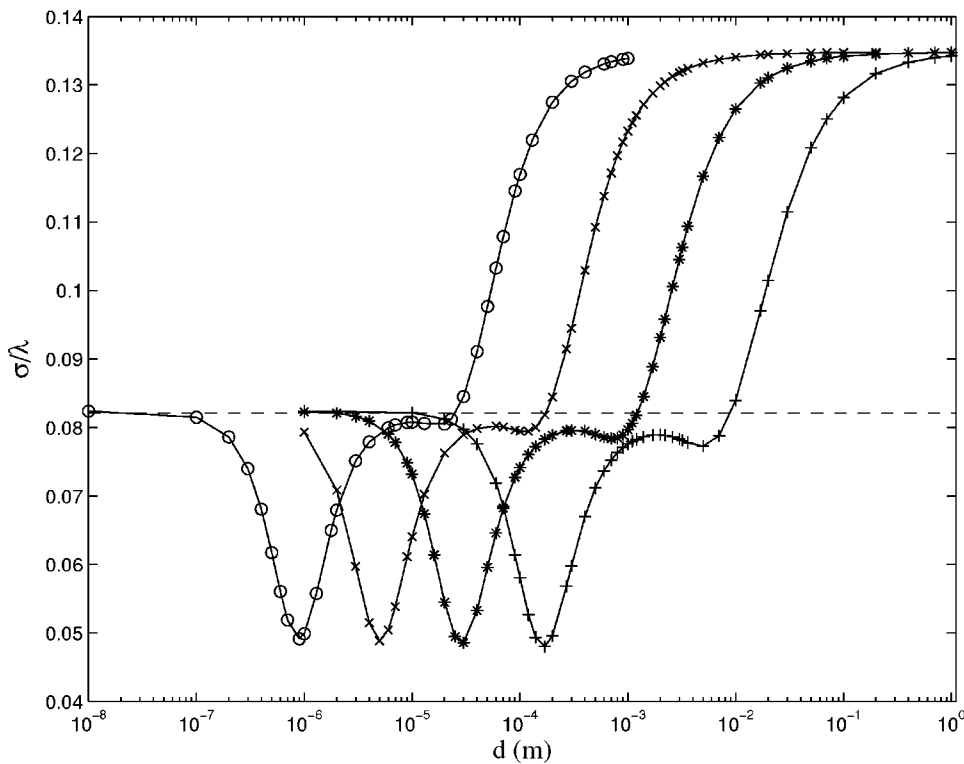


FIG. 9. Standard deviation  $\sigma/\lambda$  vs SG2 particle diameter. The standard deviation is computed using the  $x$  locations of those particles lying closest to  $x/\lambda=0.5$ . Each plot is for a different wavelength:  $\circ$ -  $\lambda=5\ \mu\text{m}$ ,  $\times$ -  $\lambda=50\ \mu\text{m}$ ,  $*$ -  $\lambda=500\ \mu\text{m}$ , and  $+$ -  $\lambda=5\ \text{mm}$ . The horizontal dashed line is the standard deviation of the massless particles,  $\sigma/\lambda=0.082141$ .

wavelength ( $\lambda=5\ \text{mm}$ ) combination, the result approaches an asymptotic value at about 1000 iterations per period for both the massless and SG2 particles.

### III. RESULTS

An example simulation is presented in Figs. 7(a)–7(d) showing the locations of 90 massless particles and 90 SG2 particles as they travel vertically downward through the oscillating boundary layers. The initial locations of both sets of particles are identical, as indicated in Fig. 7(a). The positions of these particles after 200, 300, and 400 wave cycles are presented in Figs. 7(b)–7(d), respectively. In this simulation the wavelength is 5 mm, the fluid thickness is 2.75 mm, and the diameter of the SG2 particles is  $d=170\ \mu\text{m}$ . The SG2 particles follow a different path than the massless particles, clustering closer together at the accumulation points. As will be shown below, this behavior changes with the diameter of the SG2 particles and with the liquid layer thickness. Note that the domain presented in Fig. 7 and subsequent figures which show particle locations, is a very small fraction of the total liquid layer thickness; it is this region where the boundary layer profiles presented in Figs. 1–3 show significant changes with depth and have a significant effect on particle deposition.

As noted in Sec. II, the settling velocities of the SG2 particles and the massless particles are forced to be the same. Figure 7(d) reveals that, in spite of this, the final locations of the massless particles and the SG2 particles differ due to the effect of inertia on the SG2 particles. For the case presented in Fig. 7(d), the SG2 particles cluster closer together than the massless particles. To quantify the degree of clustering, the standard deviation  $\sigma$  was computed for both groups of particles. Here  $\sigma$  is the standard deviation of the  $x$  locations of

the particle group about the accumulation point. To facilitate comparison among cases, the standard deviation was scaled to the wavelength, i.e.,  $\sigma/\lambda$ . Since the particles migrate toward a final location at either of the three accumulation points in the domain,  $x/\lambda=0, 0.5$  or  $1.0$ , each of which behaves the same as the other, only the standard deviation of those particles accumulating about one of these nodes needs to be computed. The standard deviation was computed using only those particles closest to  $x/\lambda=0.5$ . Plots of  $\sigma/\lambda$  versus  $d$  are presented in Fig. 9 for the four different wavelengths that were simulated,  $\lambda=5\ \mu\text{m}$ ,  $50\ \mu\text{m}$ ,  $500\ \mu\text{m}$ , and  $5\ \text{mm}$ , which correspond to liquid layer thicknesses of  $H=2.75\ \mu\text{m}$ ,  $27.5\ \mu\text{m}$ ,  $275\ \mu\text{m}$ , and  $2.75\ \text{mm}$ . Note that, as described above, the fluid thickness was set to  $H=0.55\lambda$ . Because the massless particles cluster in the same way regardless of the SG2 particle characteristics, the value of  $\sigma/\lambda$  remains constant for them. The horizontal line in Fig. 9 is  $\sigma/\lambda$  for the massless particles which does not change with  $\lambda$ . The plots presented in Fig. 9 display a global minimum, the significance of which is discussed below. To the right of this minimum, the particle diameters eventually extend into a nonphysical region, i.e., a region where the particle diameter exceeds the liquid film thickness. The plots are extended into this region solely to illustrate the limiting infinite diameter behavior.

Figure 9 reveals several important characteristics of particle settling. First consider the behavior of very small and very large particles. Using the  $\lambda=5\ \mu\text{m}$  plot as an example, for small particle diameters ( $d\rightarrow 10^{-8}\ \text{m}$ ), the values of  $\sigma/\lambda$  for the SG2 particles and massless particles are identical. This is expected, since the SG2 particles are themselves approaching massless behavior. For large diameters ( $d\rightarrow 10^{-2}$ ) the oscillatory boundary layers have a smaller and

smaller effect on the particle trajectory until the particles fall straight down and display a value of  $\sigma/\lambda$  independent of  $d$ . This only occurs in a nonphysical regime where  $d$  is larger than the liquid film thickness. Therefore, for all practical purposes, the oscillatory boundary layers have some finite effect on the particle deposition locations for all diameters, at least for a particle having a specific gravity of 2.0, as considered here.

Another important characteristic of Fig. 9 is the existence of two local minima in each of the four plots. The global minimum appears to be of equal magnitude for all four  $\lambda$  considered. The existence of a global minimum indicates that settling particles are maximally clumped together by the velocity field when the particle diameter is at neither its largest or smallest value, but rather at an intermediate value of  $d$ . The other local minimum appears to be more pronounced as  $\lambda$  increases, however, this minimum is of purely academic interest since the diameter at which it occurs is in the region where the diameters are nonphysical (the diameters are comparable to or larger than the film thickness).

Finally, all four of the  $\sigma/\lambda$  versus  $d$  plots are very similar in appearance and it seems that by scaling  $d$  to some value, all four would overlap. Such a scaling is not achieved using  $\lambda$ , however, since the location of the global minimum shifts by less than a factor of 10 when moving from plot to plot, while  $\lambda$  changes by exactly 10. To ascertain the similarity of all four plots, the diameter  $d_{\min}$  at which the global minimum occurred in each plot was used to scale  $d$  for each plot. Figure 10(a) presents  $d_{\min}$  plotted against  $\lambda$ . Figure 10(b) presents the data from Fig. 9 replotted with  $d$  scaled to  $d_{\min}$ . As the figure illustrates, the data collapse quite well, with only small deviations observed at large  $d$ .

#### IV. DISCUSSION

A more detailed picture of what causes the  $\sigma/\lambda$  behavior presented in Figs. 9 and 10 can be obtained using particle trajectories. Sample trajectories of particles were stored during the settling process and are plotted in Fig. 11. In each of Figs. 11(a)–11(f) a different SG2 particle diameter is considered, ranging from 10  $\mu\text{m}$  to 1 cm. The trajectories of the massless particles are, as expected, identical for each frame. Note that frames (e) and (f) present trajectories for a 1 mm and a 1 cm particle, which are nonphysical results since the film thickness is only 2.75 mm. They are included to illustrate the limiting case behavior.

Figure 11(a) shows particle trajectories that are identical for both the SG2 and massless particles. Hence, for an SG2 particle having a diameter of 10  $\mu\text{m}$ , the particle behaves as if it has no inertia and follows the flow perfectly; the trajectories and final locations coincide for both particle types. The trajectories show a general sweeping of the particles toward the accumulation points as they fall, which is caused by the asymmetries in the velocity profiles described earlier. In frames (b) and (c), the SG2 particles deviate from the massless particle trajectories, and are swept closer to the center of the accumulation points than the massless particles. This behavior is due, again, to the asymmetries in the velocity pro-

files, and also to the fact that the motion of a finite mass particle is driven by the drag force which is proportional to the square of  $u_{\Delta}$  [Eq. (9)]. Hence, the fact that the velocity is larger in the forward direction than the reverse direction (for example) has a magnified effect on the net rightward motion of an SG2 particle when compared to a massless particle. This idea is further illustrated in Fig. 12 where the results of a simple simulation are presented showing the net motion of an SG2 particle in a one-dimensional oscillatory flow where for the first part of the oscillation cycle the velocity is set to +1 m/s for 1 s and then set to  $-0.01$  m/s for 100 s in the second part of the oscillation. The net fluid motion is zero, hence a massless particle experiences no net displacement for an integral number of cycles. Figure 12 shows the net displacement of an SG2 particle for 10 oscillation cycles as a function of the diameter. This displacement increases with diameter when the diameters are small. The net displacement begins to decrease around a diameter of 1 m due to the difficulty in accelerating such a large mass in the fixed amount of time provided by 10 oscillation cycles. The net motion for a particle having the specific gravity of gold (19.3) is also presented (gold particles are frequently used in nanoparticle research).

In Figs. 11(d) and 11(e) the SG2 particle trajectories begin to get closer to those of the massless particles again. This is due to two factors. First, as the particle mass gets larger, the trajectory moves away from the curved path of Figs. 11(b) and 11(c) and more toward a straight vertical path. This is even more true in frame (f). A second factor has to do with a detail of the asymmetric velocity profiles. Referring to Fig. 3, for example, the velocity profile shows a net rightward asymmetry. However careful observation reveals that this is in fact true for  $z/\delta \gtrsim 1$ . For  $z/\delta \lesssim 1$  there is a very slight leftward asymmetry. This will contribute to forcing the SG2 particles to curve back toward the path of the massless particles for small  $z/\delta$ . This is seen in Figs. 11(d) and 11(e).

The above explanation of the particle trajectory behavior is necessarily imperfect in providing an intuitive feel for the particle behavior. The path taken by these particles is a complicated function of the mass and diameter of the particle and the complicated velocity profiles which vary with  $x$ ,  $y$  and time.

The deposition results presented here are all one-dimensional while the actual Faraday film patterns created by the process described here are two-dimensional in nature (e.g., Fig. 5). Extension of these results to two dimensions would require simulation of two components of the oscillating boundary layer velocities, rather than just the one component. Hence, extension of the  $u$ -direction boundary layer equation of Lin *et al.*<sup>3</sup> [Eq. (3)] would be necessary. One-dimensional simulations were performed to avoid the additional complexity and computational time necessary to obtain two-dimensional results. The one-dimensional results presented here, however, are useful in that they show the same qualitative behavior that would exist for the two-dimensional case. If one imagines concentration profiles corresponding to line sections through the image presented in Fig. 5, one can see that the accumulation patterns for the two-dimensional case would be much like that presented in

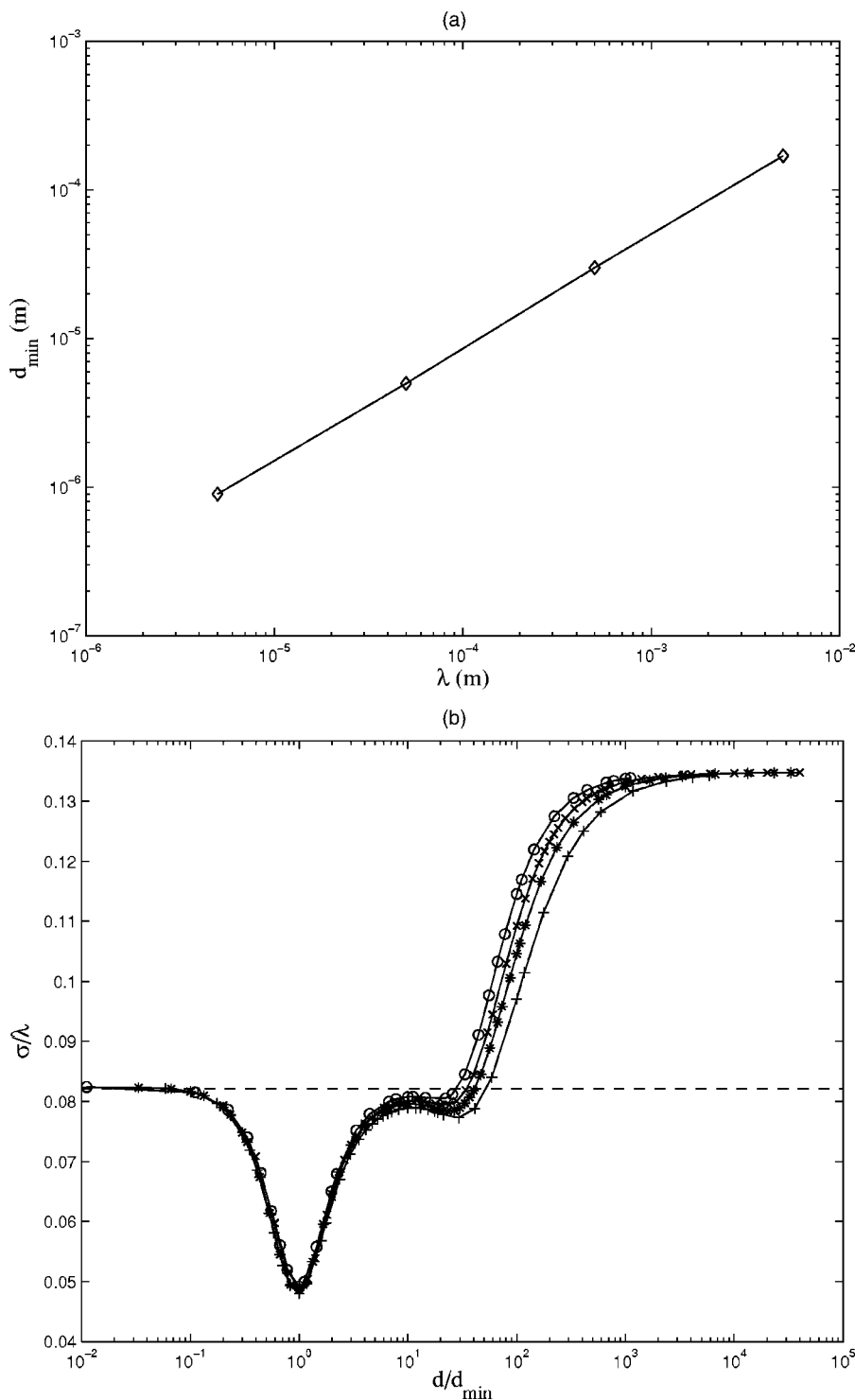


FIG. 10. (a) Plot of the diameter at which a global minimum in  $\sigma/\lambda$  is observed  $d_{\min}$  plotted against  $\lambda$ . (b)  $\sigma/\lambda$  from Fig. 9 replotted against  $d/d_{\min}$ . Symbols are the same as in Fig. 9.

Fig. 7, with each successive line section modulated in intensity.

This paper focuses primarily on the performance of this method as determined by such fluid mechanical characteristics as liquid film thickness, particle diameter, etc. Actual implementation of the method requires attention to certain practicalities that go beyond the scope of this work, but are explored in a preliminary fashion below.

Four different wavelengths were explored in this work:  $5 \mu\text{m}$ ,  $50 \mu\text{m}$ ,  $500 \mu\text{m}$ , and  $5 \text{mm}$ . The liquid film thickness and wave amplitude were set to fixed fractions of this wave-

length, as described in Sec. II (thickness,  $H=0.55\lambda$ ; amplitude  $2h=0.1\lambda$ ). This was done to provide a clear view of how the particle deposition behavior was affected by the main length scale of the system. In a practical application of this method to micron-scale patterns, adhering to these values of liquid thickness and wave amplitude becomes unrealistic, however. Table I presents the values of wave frequency, amplitude and fluid thickness that correspond to each of the four values of  $\lambda$  considered in this work showing that MHz frequencies are needed to achieve micron scale patterns. While MHz frequencies have been used to generate Faraday

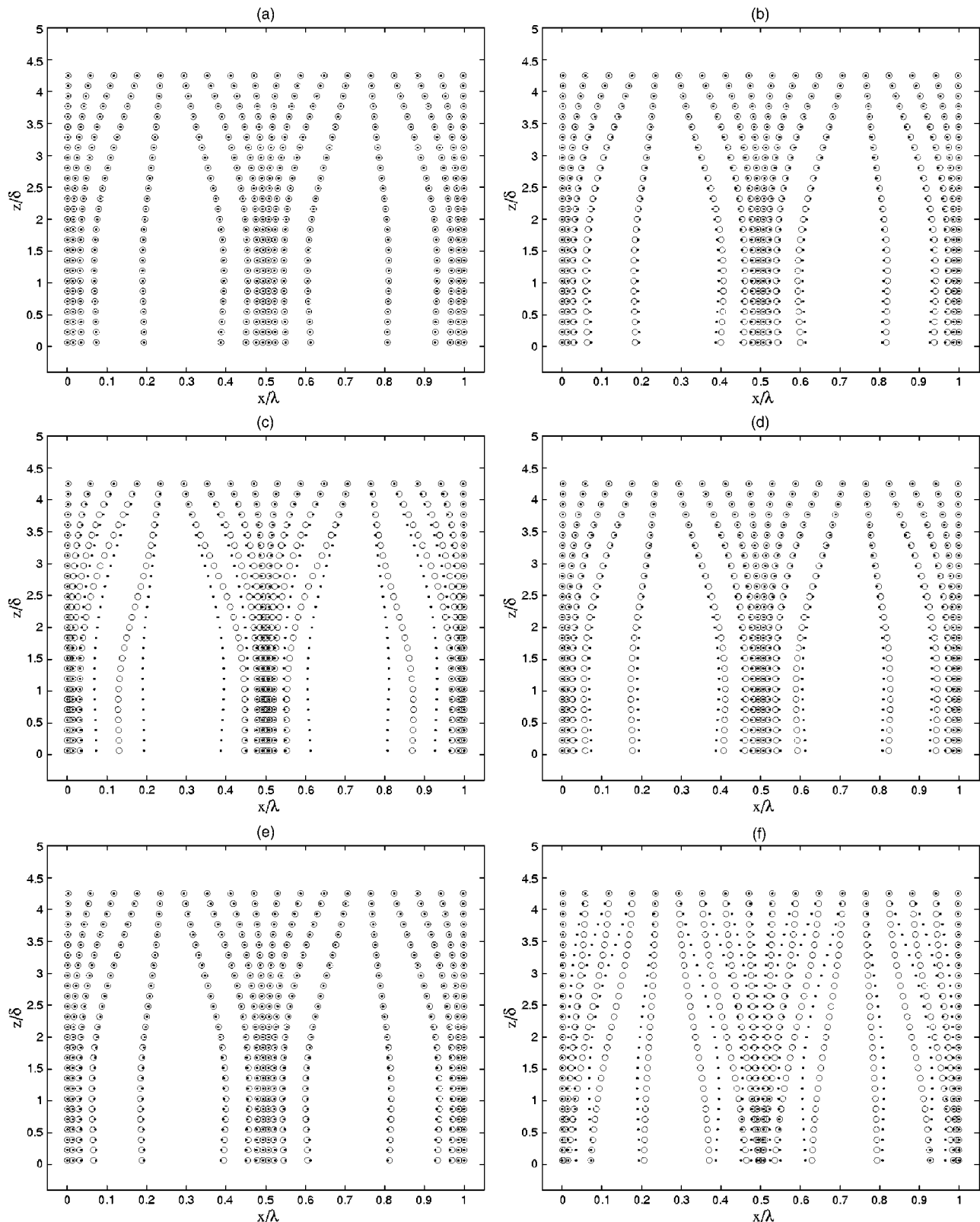


FIG. 11. Trajectories of massless ( $\bullet$ ) and SG2 ( $\circ$ ) particles in a water film having a thickness of 2.75 mm and a wavelength of 5 mm. Each frame shows the positions of the particles in the process of falling toward the surface. Each frame differs only in the diameter of the SG2 particle: (a) 10  $\mu\text{m}$ , (b) 50  $\mu\text{m}$ , (c) 170  $\mu\text{m}$ , (d) 500  $\mu\text{m}$ , (e) 1 mm, (f) 1 cm. Frames (e) and (f) present results for a nonphysical particle diameter, but are shown to illustrate limiting behavior.

waves (e.g., Eisenmenger<sup>17</sup>), such frequencies result in accelerations that are unrealistic if the wave amplitude is fixed to a value of  $0.1\lambda$ . This can be ameliorated by reducing the wave amplitude, but then one risks creating a wave field that

does not create a significant oscillatory boundary layer near the solid substrate, unless the liquid layer thickness is also reduced. Hence, in order to practically realize the patterning of particles at the micron scale using this method, one would

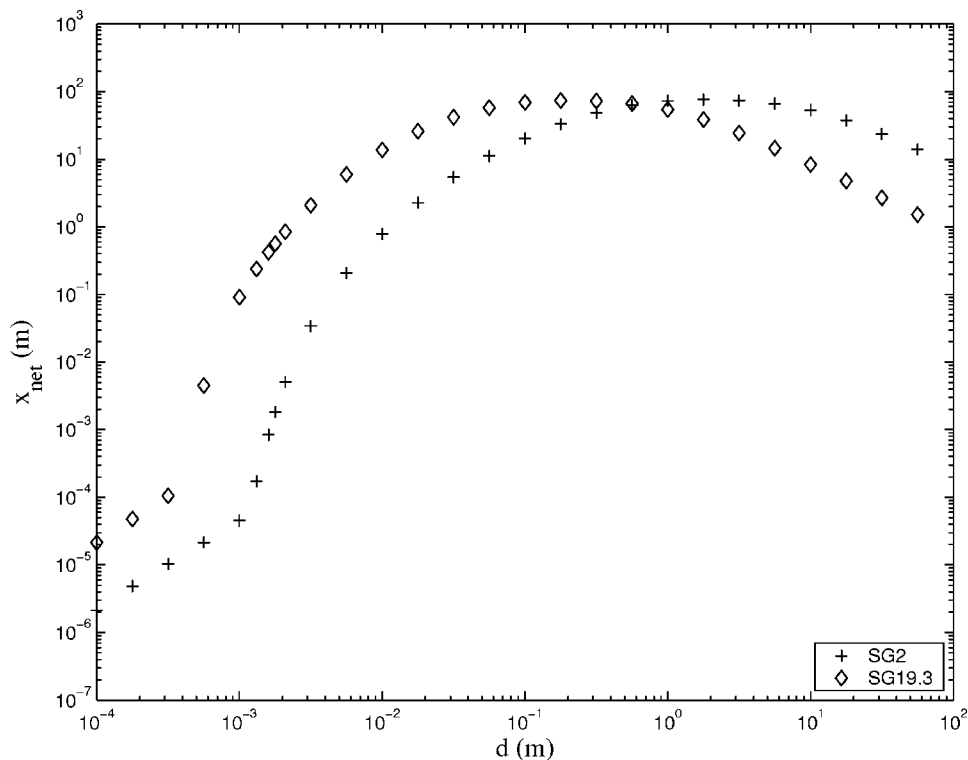


FIG. 12. Net motion of a particle experiencing a one-dimensional oscillatory velocity, where the velocity is 1 m/s in the forward direction for 1 s and 0.01 m/s in the reverse direction for 100 s. The net motion  $x_{\text{net}}$  after 10 of these cycles is plotted as a function of the particle diameter. Particles having a specific gravity of 2 and 19.3 are included.

require wave amplitudes and liquid layer thicknesses that are significantly smaller than those used in the simulations presented here.

One of the practical applications of this work, mentioned earlier, is the patterning of nanoparticles, which present some challenges. One of these is Brownian motion. When dealing with nanoscale particles, the spreading of particles due to Brownian motion can potentially blur any pattern, such as one formed using the method described here. In liquids, we can approximate Brownian motion of nanoscale particles using the diffusion coefficient,<sup>18</sup>

$$D = \frac{kT}{3\pi\mu d}, \quad (18)$$

where  $k$  is the Boltzmann constant,  $T$  is temperature,  $\mu$  is the absolute viscosity of the liquid film, and  $d$  is the diameter of the particle. Using water as the liquid and considering a particle having a diameter of 100 nm, one obtains  $D=4.4 \times 10^{-12} \text{ m}^2/\text{s}$  at  $T=300 \text{ K}$ . The characteristic diffusion length

$$L = \sqrt{Dt} \quad (19)$$

is about  $2 \mu\text{m}$  under these conditions for a time interval of one second. This would blur a Faraday film pattern created, for example, using  $5 \mu\text{m}$  Faraday waves to pattern 100 nm particles. However, it is possible to create these films in a time period significantly less than one second. Again, for the case of  $5 \mu\text{m}$  Faraday waves, the liquid thickness used in the present simulations was only  $2.75 \mu\text{m}$  (see Table I) and could be smaller. Forcing the particles to settle in a time period significantly less than one second could be achieved without requiring large settling velocities. For example, in these simulations the settling velocity was set according to Eq. (6) giving  $v_s=0.018 \text{ m/s}$  for the  $\lambda=5 \mu\text{m}$  case. Accordingly, the settling time would only be 0.15 ms and  $L$  from Eq. (19) would only be 0.3 nm for  $D=4.4 \times 10^{-12} \text{ m}^2/\text{s}$ , resulting in negligible blurring of a Faraday film comprised of 100 nm particles. Of course further Brownian motion could occur once the particles were deposited, but adhesion of the particle to the substrate due, for example, to electrostatic attraction could be used to prevent this.

As the particle diameter becomes smaller, Brownian motion becomes progressively more important and will eventually prevent the use of this method. Hence Brownian motion will serve to set the minimum diameter particle which could be used in this method for a given  $\lambda$ . A measure of this minimum diameter  $d_{\text{min}}$  for the conditions considered in the current simulations can be obtained by setting  $L=\lambda$  in Eq. (19). By combining Eqs. (5), (6), (18), and (19), and solving for  $d$ , one obtains the diameter at which Brownian motion results in a diffusion length comparable to the pattern scale,

TABLE I. Parameters used in simulations. From left to right, wavelength, frequency, liquid thickness, and wave amplitude.

$\lambda$ ( $\mu\text{m}$ )	$f$ (Hz)	$H$ ( $\mu\text{m}$ )	$2h$ ( $\mu\text{m}$ )
5000	111	2750	275
500	3540	275	27.5
50	$1.11 \times 10^5$	27.5	2.75
5	$8.67 \times 10^6$	2.75	0.275

TABLE II. Values of  $d_{\min}$  for the four wavelengths considered in the current work.

$\lambda$ ( $\mu\text{m}$ )	$d_{\min}$ (nm)
5000	0.000 77
500	0.0013
50	0.002
5	0.003

thereby insuring complete blurring of the pattern. The resulting equation is

$$d_{\min} = \frac{(0.55)(400)}{4.25} \frac{kT}{3\pi\mu\lambda} \sqrt{\frac{\pi}{\nu f}} \quad (20)$$

Table II presents the values of  $d_{\min}$  obtained using Eq. (20) for the four cases considered herein using water as the liquid and a temperature of 300 K.

Another practical problem associated with applying this method to nanoparticles is that a charged field would be required in order to force deposition. In order for the field to cause particle deposition, charging of the particles would be required. This can be achieved via a variety of methods, however, obtaining the same charge for all particles is difficult. Hence, even for a monodisperse distribution of particle diameters and uniform shapes, variations in charging would result in a distribution of settling rates. The consequence of this would be a blurring of the Faraday film pattern. For example, if one were to select a particle diameter that gives a minimum in the rms of particle spreading, as shown in Fig. 9, for the expected settling rate and liquid film thickness, variations in the actual settling velocity would result in a “detuning” of the deposition so that the particles would not accumulate at the accumulation points as well as expected. This would visually manifest as a blurring of the pattern.

The velocity field beneath a standing wave decays rapidly with distance from the liquid surface. Below a depth of one wavelength, the velocity field is negligible. Hence to utilize small scale Faraday waves to make small scale particulate patterns, a practical problem which arises concerns the ability to maintain liquid films whose thickness is comparable to the Faraday wavelength being employed. At wavelengths down to a few hundred microns this is straightforward. However, for micron scale patterns surface tension effects can cause thin films to breakdown into isolated liquid regions, and high surface tension liquids in general may not be suitable. Low surface tension liquids, such as acetone can be employed, however, their volatility makes difficult the maintenance of such a film over a reasonable period of time, requiring environmental controls capable of maintaining a saturated vapor space above the liquid film. If this is done, however, thin liquid films could be generated by slow condensation onto a temperature-controlled solid substrate.

## V. CONCLUSION

Computational simulations were presented of particle deposition beneath shallow, standing capillary waves. The simulations showed that the characteristics of the pattern created by particles settling in thin liquid films can be controlled by the particle diameter, the particle density, the wavelength, and the liquid film thickness. It was shown that an optimal particle diameter exists for a given liquid thickness and wavelength for which the accumulation of particles is maximized in the final particulate pattern. The accumulation of these particles was quantified by the standard deviation of the final particle locations about the accumulation points. This standard deviation was plotted against particle diameter, showing a minimum value. These plots showed similar behavior and were easily scaled to overlap with each other. This method has been implemented by creating a Faraday wave field on the surface of a thin liquid/particulate mixture.<sup>1</sup> The present work shows that there are many ways to control the characteristics of the particulate films obtained from this method. Some complications associated with the practical implementation of this method were discussed.

<sup>1</sup>P. H. Wright and J. R. Saylor, “The patterning of particulate films using Faraday waves,” *Rev. Sci. Instrum.* **74**, 4063 (2003).

<sup>2</sup>M. Miche, “Mouvements ondulatoires de la mer en profondeur constante ou décroissante,” *Ann. Ponts Chaussees* **144**, 25 (1944).

<sup>3</sup>C. Lin, D. S. Jeng, and C. N. Jeng, “An experimental study on the flow characteristics of a standing wave: Application of FLDV measurements,” *Ocean Eng.* **29**, 1265 (2002).

<sup>4</sup>H. Noda, “A study on mass transport in boundary layers in standing waves,” in *Proceedings of the 11th International Conference on Coastal Engineering (London)* (ASCE, Washington, DC, 1968), pp. 227–247.

<sup>5</sup>K. F. Leong, C. M. Cheah, and C. K. Chura, “Solid freeform fabrication of three-dimensional scaffolds for engineering replacement tissues and organs,” *Biomaterials* **24**, 2363 (2003).

<sup>6</sup>M. C. Roco, “Nanoparticles and nanotechnology research,” *J. Nanopart. Res.* **1**, 1 (1999).

<sup>7</sup>M. C. Roco, “Towards a US national nanotechnology initiative,” *J. Nanopart. Res.* **1**, 435 (1999).

<sup>8</sup>N. Saito, H. Haneda, and K. Koumoto, “Pattern-deposition of light-emitting ZnO particulate film through biomimetic process using self-assembled monolayer template,” *Microelectron. J.* **35**, 349 (2004).

<sup>9</sup>D. R. Rainer, C. Xu, and D. W. Goodman, “Characterization and catalysis studies of small metal particles on planar model oxide supports,” *J. Mol. Catal. A: Chem.* **119**, 307 (1997).

<sup>10</sup>F. M. White, *Viscous Fluid Flow*, 2nd ed. (McGraw-Hill, Boston, MA, 1991).

<sup>11</sup>G. A. Voth, B. Bigger, M. R. Buckley, W. Losert, M. P. Brenner, H. A. Stone, and J. P. Gollub, “Ordered clusters and dynamical states of particles in a vibrated fluid,” *Phys. Rev. Lett.* **88**, 234301 (2002).

<sup>12</sup>E. C. Eckstein, D. G. Baile, and D. G. Shapiro, “Self-diffusion of particles in shear flow of a suspension,” *J. Fluid Mech.* **79**, 191 (1977).

<sup>13</sup>D. Leighton and A. Acrivos, “Viscous resuspension,” *Chem. Eng. Sci.* **41**, 1377 (1986).

<sup>14</sup>D. Leighton and A. Acrivos, “Measurement of shear-induced self-diffusion in concentrated suspensions of spheres,” *J. Fluid Mech.* **177**, 109 (1987).

<sup>15</sup>D. Leighton and A. Acrivos, “The shear-induced migration of particles in concentrated suspensions,” *J. Fluid Mech.* **181**, 415 (1987).

<sup>16</sup>G. Dietrich, *General Oceanography* (Wiley, New York, NY, 1963).

<sup>17</sup>W. Eisenmenger, “Dynamic properties of the surface tension of water and aqueous solutions of surface active agents with standing capillary waves in the frequency range from 10 kc/s to 1.5 Mc/s,” *Acustica* **9**, 327 (1959).

<sup>18</sup>A. F. Mills, *Mass Transfer* (Prentice Hall, Upper Saddle River, NJ, 2001).